Production of nanoemulsions using anodic alumina membranes in a stirred-cell setup

Maria Medina-Llamas[a] and Davide Mattia[a*]

[a] Chemical Engineering Department, University of Bath, Claverton Down, BA2 7AY, Bath, United Kingdom

Abstract

Oil-in-water nanoemulsions (NEs) were produced in a dead-end stirred cell setup for the first time using bespoke anodic alumina membranes (AAMs). The regular pore structure and narrow pore size distribution of AAMs enabled the formation of NEs with narrow size distributions. Rotational speed and membrane pore size were the key parameters in controlling the droplet size, with droplets as small as 144 ± 18 nm obtained using a membrane with a pore size of 58 ± 6 nm. Low values of the droplet diameter-to-pore diameter ratio, ranging from 1.8 to 3.5 were obtained, compared to typical literature values of ~10. Literature droplet size prediction models for micro-emulsions overestimate results by up to ~ 600 %, whereas a model developed by the authors for NEs is much closer to experimental values. These results show that stable and controlled NEs can be produced for a variety of applications - ranging from consumer products to materials manufacturing - and, potentially, at large scale.

Keywords: membrane emulsification, anodic alumina membrane, nanoemulsion, stirred tank, oil-in-water emulsion, modelling.

Abbreviations: AAMs, anodic alumina membranes; DW, deionized water; HLB, hydrophilic-lipophilic balance; ME, Membrane emulsification; NEs, Nanoemulsions; SFO, Sunflower oil.

*corresponding author: d.mattia@bath.ac.uk

1. Introduction

Nanoemulsions have been considered for a wide range of promising applications due to their optical transparency, their high surface area and their kinetic stability. These applications include, among others, an enhanced bioavailability of lipophilic compounds as drug delivery systems in the pharmaceutical industry;[1] the incorporation of nutraceuticals, vitamins, colours and flavours in the food and cosmetic sectors;[1] pesticide formulations;[2] and as a reactor media for the production of nanoparticles.[3]

A NE is a two-phase system of immiscible liquids in which one liquid is dispersed as small droplets in the other one.[4] NEs can be distinguished by their preparation methods, their physical properties and their kinetic stability.[5] However, the size boundaries of NEs are not clearly defined, with some defining NEs having dispersed phase diameters from 20 nm to 200 nm,[6] while others set 500 nm as an upper diameter limit.[7] Furthermore, NEs can be prepared by low-energy and high-energy methods. The former are non-mechanical processes where the NE formation is caused by a sudden change in the composition or temperature.[8] On the other hand, high-energy methods require a considerable energy input to produce the emulsion and include rotor-stator and ultrasound systems, high-pressure homogenizers and microfluidizers.[5]
Membrane emulsification (ME) is a low-energy mechanical process, with several advantages compared to high-energy ones: First, the dispersed phase droplets are generated by the permeation of the disperse phase through the membrane pores, and not by the disruption of a coarse emulsion, which leads to the production of droplets with narrower size distribution. In addition, ME requires lower energy inputs in the order of 10^4 - 10^6 J/m^3 compared to other methods requiring 10^6 - 10^8 J/m. [3, 9] Finally, the size of the resulting dispersed phase droplets is

mainly determined by the membrane pore size and the fluid dynamics of the system, both of which can be well controlled.

It has been widely reported that a linear relation exists between the membrane pore diameter and the average droplet diameter in ME:

$$D_d = cD_p \quad (1)$$

where D_d is the average droplet diameter, D_p is the average pore diameter and c is a proportionality constant related to the membrane structure and material. Reported c values range between 2 and 10 for Shirasu Porous Glass (SPG) membranes and from 2 to 50 for other types of membranes with a less regular pore structure.[10] Droplets smaller than the membrane pore (with a fractional c value) have also been obtained using a tubular SPG membrane, but with a wide size distribution.[11] SPG membranes are the most extensively explored material in ME. They are hydrophilic membranes with low tortuosity and interconnected pores ranging from 0.05 to 30 μm.[10]

Anodic alumina membranes (AAMs) can be described as highly ordered porous structures in a hexagonal arrangement with narrow pore size distributions.[12] They are synthetized by the electrochemical oxidation of aluminium in mild anodization conditions.[13] One of their main features is that pore size can be tuned by altering the anodization conditions from about 5 to 300 nm, depending on the anodization voltage and electrolyte type.[12,14] Moreover, the low porosity of AAMs, 8 - 30 %,[15] compared with 50 – 60 % for SPG membranes,[10] reduces the risk of coalescence between droplets, making it possible to achieve monodispersed emulsions. These characteristics, and the fact that they are hydrophilic,[16] make AAMs suitable for the preparation of oil-in-water NEs, although different surface modification approaches have been conducted[18] e.g. prepare hydrophobised AAMs suitable for water-in-oil emulsions.[16,17]

1.1 Droplet detachment model

The production of a dispersed phase droplet in ME involves two stages, *droplet growth* and *droplet detachment,*[18] where the final size of the droplet is dependent on a balance of the forces acting on the droplet during both stages. The interfacial tension force, F_γ, representing the adhesion of the dispersed phase at the edge of the pore, is:

$$F_\gamma = 2\pi\gamma r_p \tag{2}$$

where γ is the interfacial tension force and r_p is the pore radius. The drag force, F_D, caused by the movement of the continuous phase at the edge of the membrane pore and the main force responsible for the detachment of the droplet is:

$$F_D = 6k_x\pi\tau r_d^2 \tag{3}$$

where r_d is the droplet radius, k_x is a correction factor and τ is the shear stress. The buoyancy force, F_B, caused by the difference in density between the continuous and the dispersed phase is expressed as:

$$F_B = \frac{4}{3}\pi r_d^3(\rho_c - \rho_d)g \tag{4}$$

where, g is the gravitational constant and ρ_c and ρ_d are the densities of the continuous and the dispersed phases, respectively. The inertial force, F_I, is produced by the flow of the dispersed phase from the pore tip:

$$F_I = \rho_d\pi\, r_p^2 v_d^2 \tag{5}$$

where v_d is the velocity of the dispersed phase within the pore. The static pressure force, F_{st}, is due to the pressure difference between the dispersed phase and the continuous phase at the membrane surface:

$$F_{st} = \gamma\pi\frac{D_p^2}{D_d} \quad (6)$$

For droplets in the micrometre range, inertia and buoyancy forces are approximately 9 and 6 orders of magnitude smaller, respectively, than interfacial and drag forces.[19] Therefore, they are generally neglected from force balance models. Modelling of nanoemulsions produced via ME has shown, on the contrary, that these have to be considered for the models to more accurately predict the experimental conditions.[20]

While most publications on ME reported using a crossflow configuration,[21] Kosvintsev, et al. [22] introduced the concept of a batch stirred cell for the production of emulsions with dispersed phase droplets in the micrometer scale, using a paddle-blade impeller. In a stirred tank, the shear stress has a radial profile, having their highest value at the critical radius (r_c). Along this shear stress profile, there are two regions: The first one for positions $r < r_c$, is a forced vortex region, which exhibits a rigid-body motion with an angular speed of the impeller (ω); the second is a free vortex region for, $r > r_c$, in which the angular momentum ($r\tau$) is constant.[22] The position of the critical radius can be found based on Yamamoto's method reported by Nagata:[23]

$$r_c = \frac{D}{2}1.23\left(0.57 + 0.35\frac{D}{T_D}\right)\left(\frac{b}{T_D}\right)^{0.036}\left(\frac{Re}{1000 + 1.43Re}\right)n_b^{0.116} \quad (7)$$

where D is the impeller diameter, T_D is the tank diameter, b is the blade height, n_b is the number of blades and Re is the Reynolds number:

$$Re = \frac{\rho_c \omega D^2}{2\pi\mu} \quad (8)$$

where ω is the angular speed and μ is the viscosity of the continuous phase. For each region, the shear stress at the membrane surface can be calculated using the equations:[22]

$$\tau = 0.825\mu\omega r \frac{1}{\delta} \qquad r \leq r_c \quad (9)$$

$$\tau = 0.825\mu\omega r \frac{1}{\delta} r_c \left(\frac{r_c}{r}\right)^{0.6} \qquad r > r_c \quad (10)$$

where the boundary layer thickness is defined using the equation:

$$\delta = \sqrt{\frac{\mu}{\rho_c \omega}} \quad (11)$$

While the above equations are specific to a paddle-blade configuration, other paddle geometries, including a disk-type stirrer have also been considered in the literature.[24]

In the present work, the fabrication of NEs in a stirred cell reactor using bespoke AAMs is reported for the first time. Oil-in-water NEs, consisting of sunflower oil and deionized water (DW) as dispersed and continuous phase, respectively, were prepared. The effect of the membrane pore size, injection rate, type of surfactant, rotational speed and surfactant addition in both phases was evaluated to achieve the formation of nanoemulsions with a narrow droplet size distribution. The stability of the NEs was monitored using dynamic light scattering. Finally, the experimental results were compared with droplet size estimation models available in the literature to understand the mechanism involved during the droplet formation at the nanoscale.

2. Materials and methods

2.1 Materials

High purity aluminium foil (99.99 %) with 0.25 mm thickness was purchased from Alfa Aesar. Phosphoric acid (H_3PO_4) 85 %, perchloric acid ($HClO_4$) 70 %, hydrochloric acid (HCl) 37 %, acetone (C_3H_6O) 99 %, ethanol (C_2H_5OH) 99 % and copper (II) chloride dihydrated ($CuCl_2 \cdot 2H_2O$) 99 %, all reactive grade, were purchased from Sigma Aldrich. Chromium (VI) oxide (CrO_3) 99.5 %, oxalic acid anhydrous ($C_2H_2O_4$), 98 % and sulphuric acid (H_2SO_4) 98 %, reactive grade, were purchased from Fisher Scientific. Commercial sunflower oil (SFO) for domestic use (Goldfields, Cargill UK) was used as dispersed phase. The surfactants Tween 20 and Span 80 and Brij O10 were purchased from Sigma Aldrich and Tween 80 from Fisher Scientific.

2.2 Membrane fabrication

Flat disc anodic alumina membranes were produced via a two-step anodization process. The anodization was carried out under potentiostatic conditions using oxalic acid as electrolyte and varying voltage and temperature to achieve different membrane pore sizes. A detailed description of the synthesis of AAMs can be found in the supplementary information. The final diameter of the AAMs was 10 mm; to place the membrane inside the emulsification rig, the membrane was glued between two flat outer diameter 13 mm silicone gaskets, the final active membrane diameter for the emulsification experiments was 6 mm. The morphology of the AAMs was studied via FESEM (JEOL JSM 6330F) and the obtained micrographs were analysed using an image processing software (ImageJ) to determine the average pore diameter, interpore distance, porosity and pore density.

2.3 Membrane emulsification apparatus and experiments

Oil-in-water NEs were produced using a dead-end 3D-printed membrane emulsification rig with an overhead stirrer (IKA, RW 11). The membrane emulsification rig (Figure 1a) consisted of a 50 ml tank filled with 25 ml of continuous phase (1 % wt. Tween 20 in DW). The tank (internal diameter 6 mm) was connected at the base to a 13 mm membrane holder (Millipore) where the AAM was placed. The membrane was flush with the base of the tank, leaving an exposed membrane area of 6 mm in diameter. A syringe pump (KR analytical, Nexus 200) was used to push the dispersed phase, 4 % wt. Span 80 in SFO, through the membrane pores. The shear stress was provided via the overhead stirrer (IKA, RW 11) with a 5 mm diameter, 3 mm thick and 4 mm high paddle-blade impeller at different rotational speeds ranging from 100 to 1750 rpm. The droplet size distribution of the NEs was analysed via dynamic light scattering (DLS) in backscattering mode with a detection angle of 173° (Zetasizer Nano-ZS, Malvern Instruments). Droplet size distributions are presented as light scattered intensity % vs. droplet size, without any manipulation of data from the DLS.[25, 26] The density and viscosity values of the dispersed phase at 20 ˚C are 0.92 g ml^{-1} and 49 mPa s, respectively. The values for the same quantities for the

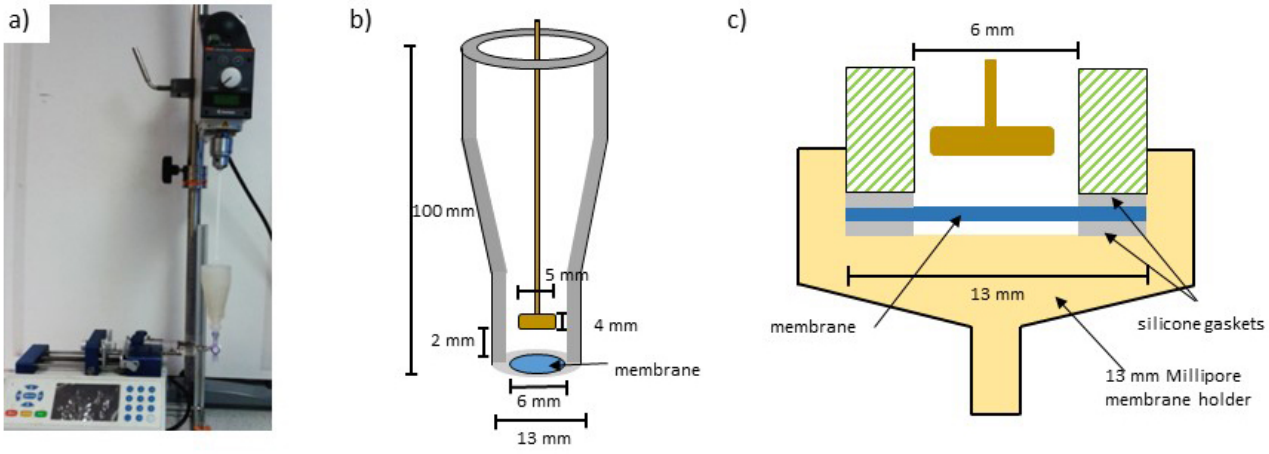

Figure 1. a) Membrane emulsification apparatus; b) dimensions of the tank; and c) close-up of the membrane holder and paddle-blade impeller.

continuous phase are 0.99 g ml-1 and 1.00 mPa s, respectively. The final concentration of the dispersed phase in the nanoemulsion was 0.6 %vol. After the formation of each NE, each membrane was cleaned using acetone, ethanol and water in sequence under sonication for 15 minutes and at least four consecutive times for each solvent. After the cleaning process, the membranes were sonicated for 10 minutes in the continuous phase. The rig dimensions are shown in Figure 1b. The molecular weight and HLB value of the surfactants used can be found in Table 1.

Table 1. Molecular weight and HLB value of selected surfactants

Surfactant	Molecular weight/g mol^{-1}	HLB
Brij O10	709	12.4
Tween 20	1228	16.7
Tween 80	1310	15.0
Span 80	428	4.3

3. Results and discussion

3.1 Membrane morphology

One of the main reasons why AAMs are a very attractive material for nano-applications is the high pore regularity and the close-packed arrangement that can be obtained under specific reaction conditions.[14] Figure 2a is a low magnification SEM micrograph showing that hexagonal arrays are present within the material's microdomains and they are separated from adjacent domains by grain boundaries. A cross-sectional micrograph (Figure 2b) shows the formation of straight and non-interconnected pores, which are also characteristic features of AAMs. The AAMs exhibit a positive relation between the anodization potential and the pore diameter with a

proportionality constant of 1.34 nm V^{-1} (Figure 2f), a finding in good agreement with reported values in the literature (1.29 nm V^{-1}).[15] The best results in terms of pore size regularity were achieved for membranes fabricated at 40 V with oxalic acid where a self-organised pore arrangement and ideal honeycomb structures are obtained.[27] For example, by synthetizing an AAM when a 40 V potential is applied, a 58 ± 6 nm mean membrane pore size was obtained (Figure 2c). The synthesis conditions of the AAMs can be found in Table S1 in the supporting information. At higher potential, less ordered porous structures are formed and a reduction of the pore circularity is clearly observed (Figures 2d and 2e). This can be attributed to an increase of the volume expansion associated with the formation of aluminum oxide at the metal/oxide interface and a reduction of the time for the self-organized formation of hexagonal pores arrays.[28] A positive correlation between anodization potential and interpore distance was also observed with a gradient value of 2.3 nm V^{-1} close to the 2.5 nm V^{-1} value reported in literature.[29] The interpore distance, porosity, pore density and circularity values can be found in

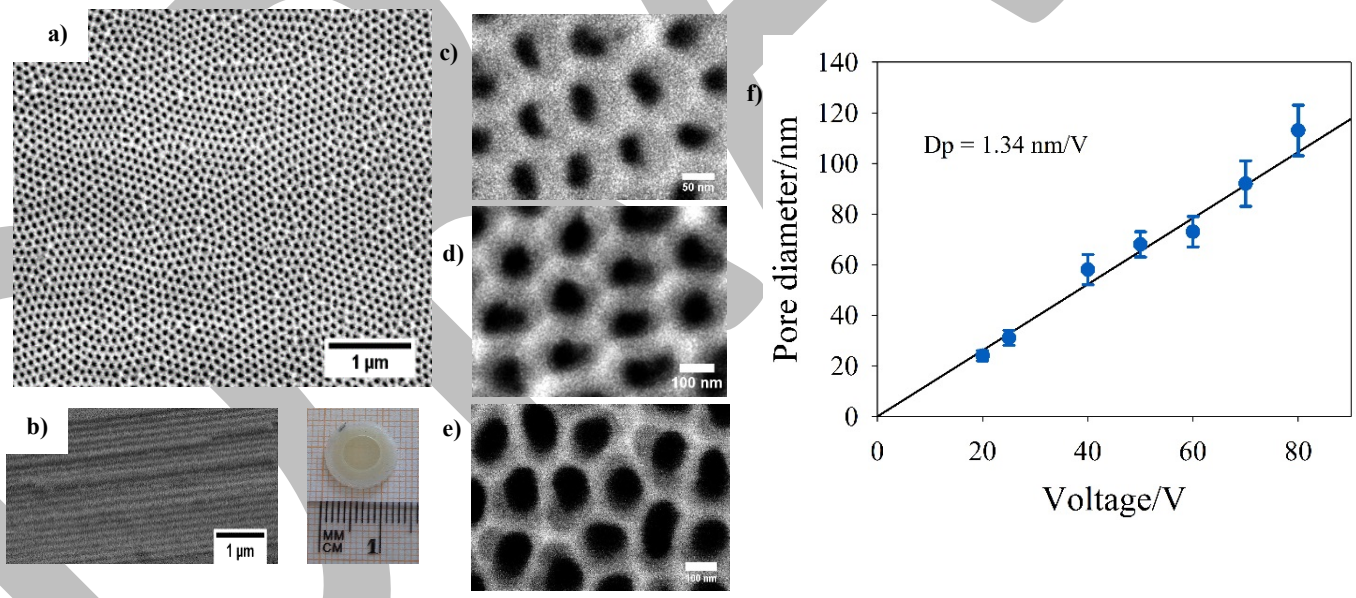

Figure 2. a) Large section of an AAM, b) cross section c), d) and e) micrographs of a 40, 70 and 80 V membranes, respectively, f) correlation between the membrane pore diameter and the anodization potential.

Table S2 in the supporting information. Permeability-selectivity tests for AAMs have been reported elsewhere.[14,30]

3.2 Nanoemulsion production

3.2.1 Effect of the surfactant addition in the dispersed phase

In membrane emulsification, the addition of a surfactant in the continuous phase stabilises the droplets against coalescence and reduces the interfacial tension between the two phases and, thus, decreases the minimum operating pressure needed to push the dispersed phase through the membrane pores. However, previous reports suggested that monodispersed emulsions can be obtained when a lipophilic surfactant is added to the oil phase and a hydrophilic surfactant is added to the water.[31] In the present work, NEs obtained when only a hydrophilic surfactant (1 % wt. Tween 20 in DW) was added to the continuous phase were compared, in terms of droplet size and size distribution, with NEs produced with surfactant in both the dispersed (4 % wt. Span 80

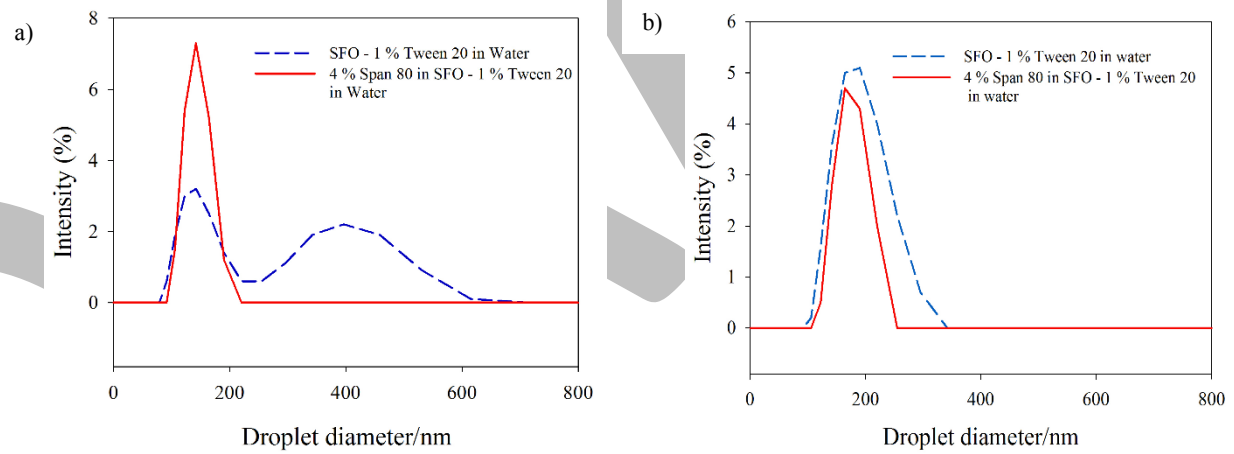

Figure 3. Intensity against droplet size for a NE formed using 1 % wt. Tween 20 as surfactant in DW and with or without the addition of surfactant (4 % wt. Span 80) in the dispersed phase (SFO) for the same conditions (0.15 ml of dispersed phase injected at 0.015 ml/min in 25 ml of continuous phase at 1750 rpm) for a) 40 V membrane (58 ± 6 nm) b) 60 V membrane (73 ± 6 nm).

in SFO) and the continuous phases (1 % wt. Tween 20 in DW). These experiments were carried out using a 40 and a 60 V membrane at different rotational speeds (100 - 1750 rpm).

For a 40 V membrane, the results show that bimodal NEs was obtained in the whole range of the rotational speeds when only a hydrophilic surfactant is added to the continuous phase (1 % wt. Tween 20). Figure 3a demonstrates this behaviour, where droplet diameters of 148 ± 39 nm and 393 ± 82 nm were obtained. Meanwhile, monomodal NEs were achieved when a 4 % wt. Span 80 was incorporated in the dispersed phase and 1 % wt. Tween 20 in the continuous phase, with a droplet size of 154 ± 19 nm. These results were obtained for the highest rotational speed (1750 rpm). Values for all experiments can be found in Table S3 in the supporting information.

On the other hand, for a 60 V membrane, monomodal NEs were produced regardless of the additional incorporation of surfactant in the dispersed phase and only slightly wider NEs were obtained at low rotational speeds when SFO was the dispersed phase (Figure 3b). The droplet diameter obtained for the complete range of rotational speeds for a 60 V membrane with and without the addition of a surfactant in the dispersed phase can be found in Figure S1.

The different behaviour for the two membranes under the same process conditions can be explained by a difference in the interpore spacing between the 60 V membrane (117 ± 10 nm) and the 40 V one (101 ± 5 nm). The former might allow adjacent droplets to grow without producing droplet coalescence. Furthermore, previous reports suggested that to avoid droplet coalescence, the incorporation of a surfactant in the dispersed phase is beneficial as this minimises the diffusional distance from the pore tip to the oil/water interface, when the droplet is growing, thereby providing a steady supply of surfactant that avoids droplet coalescence.[31] In the case of the membrane with a smaller interpore distance and no lipophilic surfactant, the bimodal distribution can be explained by droplet coalescence due to the combined effect of the small

interpore distance and the slow incorporation of the surfactant molecules (Tween 20) at the oil/water interface when the droplet is growing.

3.2.2 Effect of the type of surfactant

Three different surfactants in the continuous phase were tested to evaluate the effect of varying molecular weight (Table 1). The experiments were carried out using 40 V membranes and varying the rotational speed and the dispersed phase incorporating 4 % wt. Span 80 (Figure 4).

At a low rotational speed (100 rpm), a considerable reduction of the droplet diameter with decreasing molecular weight of the surfactant was observed. In addition, droplets with a narrower size distribution were produced. This effect can be explained in terms of the surfactant diffusion coefficients (D_s), which can be estimated using the Stokes-Einstein equation:

$$D_s = \frac{kT}{6\pi\mu D_h} \tag{11}$$

where k is the Boltzmann constant, T is temperature, μ is viscosity of the continuous phase, and D_h is the hydrodynamic diameter, which can be considered as equal to $2R_g$, the surfactant's gyration radius $\left(R_g = M_w^{0.6} \cdot 10^{-9}\right)$, and M_w is the molecular weight of the surfactant. Furthermore, the diffusion coefficient is related to the surfactant mass transfer coefficient (k_s) by:

$$k_s = \sqrt{\frac{D_s}{\pi t}} \tag{12}$$

where t is the droplet formation time.[32] The last two equations express the fact that surfactants with higher molecular weight have a larger hydrodynamic diameter and slower diffusion from the bulk of the continuous phase to the oil/water interface. A surfactant with a lower diffusion coefficient will have a lower mass transfer coefficient and will cause an increment of the droplet formation time, leading to the formation of bigger droplets and wider size distributions.

In Figure 4, it is observed that upon increasing the rotational speed, beyond a certain threshold the effect of the surfactant molecular weight on the droplet diameter becomes minimal, with only a narrowing of droplet size distribution due to the higher shear rate (as discussed below).

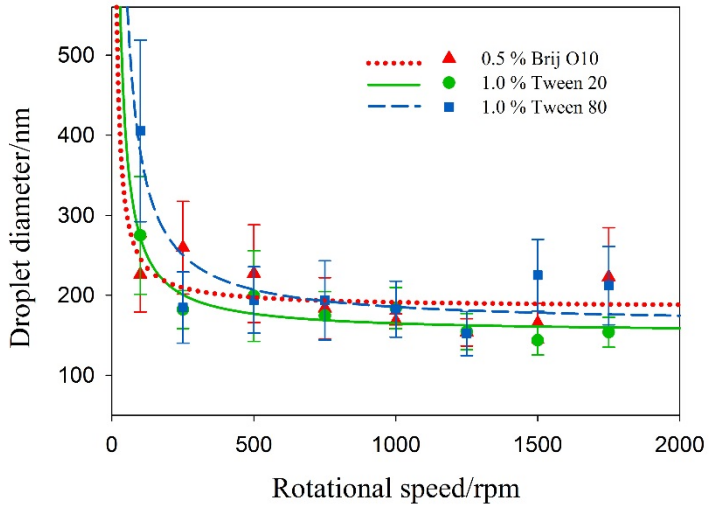

Figure 4. Droplet diameter against rotational speed for three different surfactants added in the continuous phase using a 40 V membrane (58 ± 6 nm) with R^2 value of 0.26, 0.86 and 0.78 for Brij O10, Tween 20 and Tween 80, respectively, using an inverse first order fit.

3.2.3 Effect of the injection rate

Three different injection rates (0.015, 0.030 and 0.045 ml/min) were tested using 40 and 60 V membranes for different rotational speeds (100 - 1750 rpm), Figures 5a and 5b, respectively. The surfactants were 1 % wt. Tween 20 in the continuous phase and 4 % wt. Span 80 in the dispersed phase.

The results for the 40 V membrane show that above 300 rpm there is only a weak effect of both the rotational speed and the injection rate on the droplet diameter. For the three injection rates tested, the droplet diameters lie in a range from 144 to 275 nm. However, droplets as small as

144 ± 18 nm and 154 ± 19 nm can be achieved with an injection rate of 0.015 ml/min at 1500 and 1750 rpm, respectively.

For a 60 V membrane the results show that there is a stronger influence of both the rotational speed and the injection rate over the droplet diameter at low rotational speeds, where the droplet diameter has a negative correlation with the rotational speed (Figure 5b). In this region, larger droplet diameters and wider size distributions are observed due to a combined effect of the increase of the dispersed phase flux and the insufficient drag force to produce droplet detachment. The second region occurs at higher rotational speeds, where the droplet diameter is almost independent of the injection rate and the shear stress. This region is observed at rotational speeds higher than 750 rpm where narrower droplets are obtained. This different behaviour

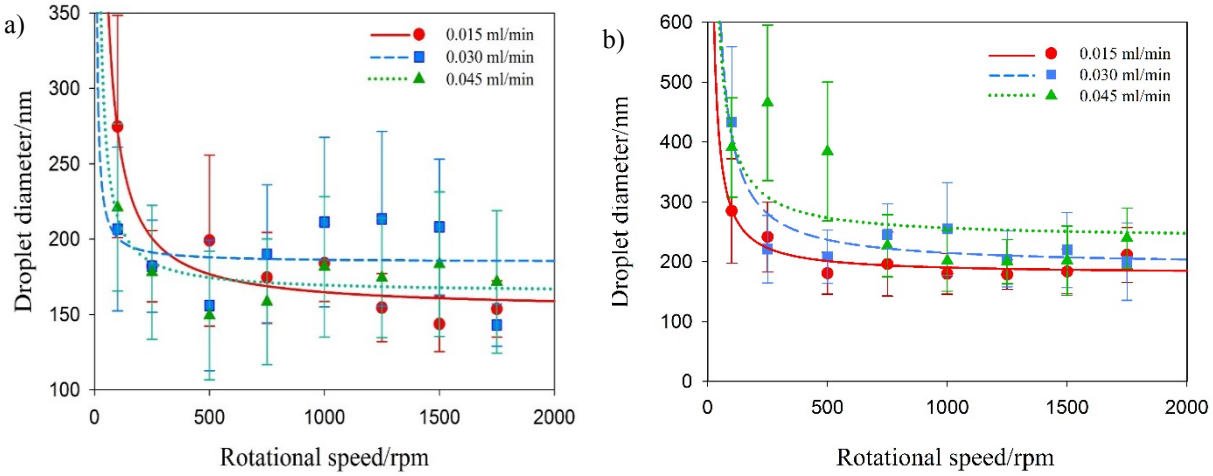

Figure 5. Droplet diameter of NEs using a) 40 V (58 ± 6 nm) and b) 60 V (73 ± 6 nm) membranes with 1 % wt. Tween 20 and 4 % wt. Span 80 as surfactant in the continuous and dispersed phase, respectively, for different rotational speeds and different injection rates. For a 40 V membrane R^2 values are 0.86, 0.11 and 0.75 for 0.015, 0.030 and 0.045 ml/min, respectively, using an inverse second order fit. For a 60 V membrane R^2 values are 0.84, 0.83 and 0.44 for 0.015, 0.030 and 0.045 ml/min, respectively, using an inverse first order fit.

between a 40 and a 60 V membrane in terms of the rotational speed and droplet size dependence is similar to what was observed previously for micrometer size droplets produced via cross-flow ME where the smaller the pore size, the smaller the shear stress value needed for droplet detachment.[33] The authors have shown something similar at the nanoscale in cross-flow configuration.[20]

3.2.4 Effect of the pore size

The effect of the membrane pore size on the droplet diameter was evaluated by fabricating AAMs at different voltages to achieve different average pore sizes (Table S1 and Figure 2f). Figure 6a shows the droplet diameter of NEs obtained by injecting 0.15 ml of dispersed phase (4 % wt. Span 80 in SFO) at 0.015 ml/min in 25 ml of continuous phase (1 % wt. Tween 20 in DW) as a function of the pore size for defined shear stress values. The results show a positive correlation between the membrane pore size and the droplet diameter. Furthermore, it is possible to identify two regions (Figure 6a and Figure 6b): The first one at low rotational speeds, where the shear stress is not high enough to produce droplet detachment and bigger droplets with wider size distribution are obtained. In this region, the sharpest decrease on the droplet diameter is observed especially at the lowest rotational speeds (100 rpm), a trend previously reported for membrane emulsification using flat membranes at the micrometer scale.[34,22] A distinct behaviour is observed at higher rotational speeds (> 1000 rpm) where the droplet diameter is nearly independent of rotational speed (Figure 6b). The behaviour of the droplet diameter at these high rotational speeds shows that the minimum value of the droplet has been reached and consequently the membrane pore size and rotational speed will be the key parameters for controlling the droplet size.

Another trend observed is that wider droplet size distributions are obtained with the increase on the membrane pore size along all the rotational speeds. The last is a consequence of the decrease on the membrane quality in terms of pore circularity, as can be seen in Figures 2c, 2d and 2e. As discussed in Section 3.1, during membrane fabrication higher potentials produce less ordered porous structures with wider pore size distributions and an increase in the pore heterogeneity. These translate into the formation of NEs with wider size distributions, an issue that cannot be overcome with an increase on the rotational speed.

As the main parameters influencing droplet size are membrane pore size and shear stress, it is convenient to express the contribution of both parameters in a single dimensionless number, the Euler number: [35]

$$Eu_{trans} = \frac{\Delta P}{\rho_c N^2 D^2}$$

Figure 6c shows the ratio of the average droplet diameter to the average pore size (D_d/D_p) for AAMs with different pore sizes, under the conditions in Figure 6a, against the rotational speed and the inverse of the Euler number for different membrane pore sizes and rotational speeds (Figure 6d). The results show the proportionality constant values lies between 1.8 and 3.5, for rotational speeds above 200 rpm. These values are small compared to the ones in the literature, which typically go up to 10 for SPG and up to 50 for other less ordered membranes.[10] Only for rotational speeds below 200 rpm, this value goes up to 4.9, for the given conditions. The low

proportionality values obtained are due to the circular pores in a highly-ordered arrangement and narrow pore size distribution of the AAMs.

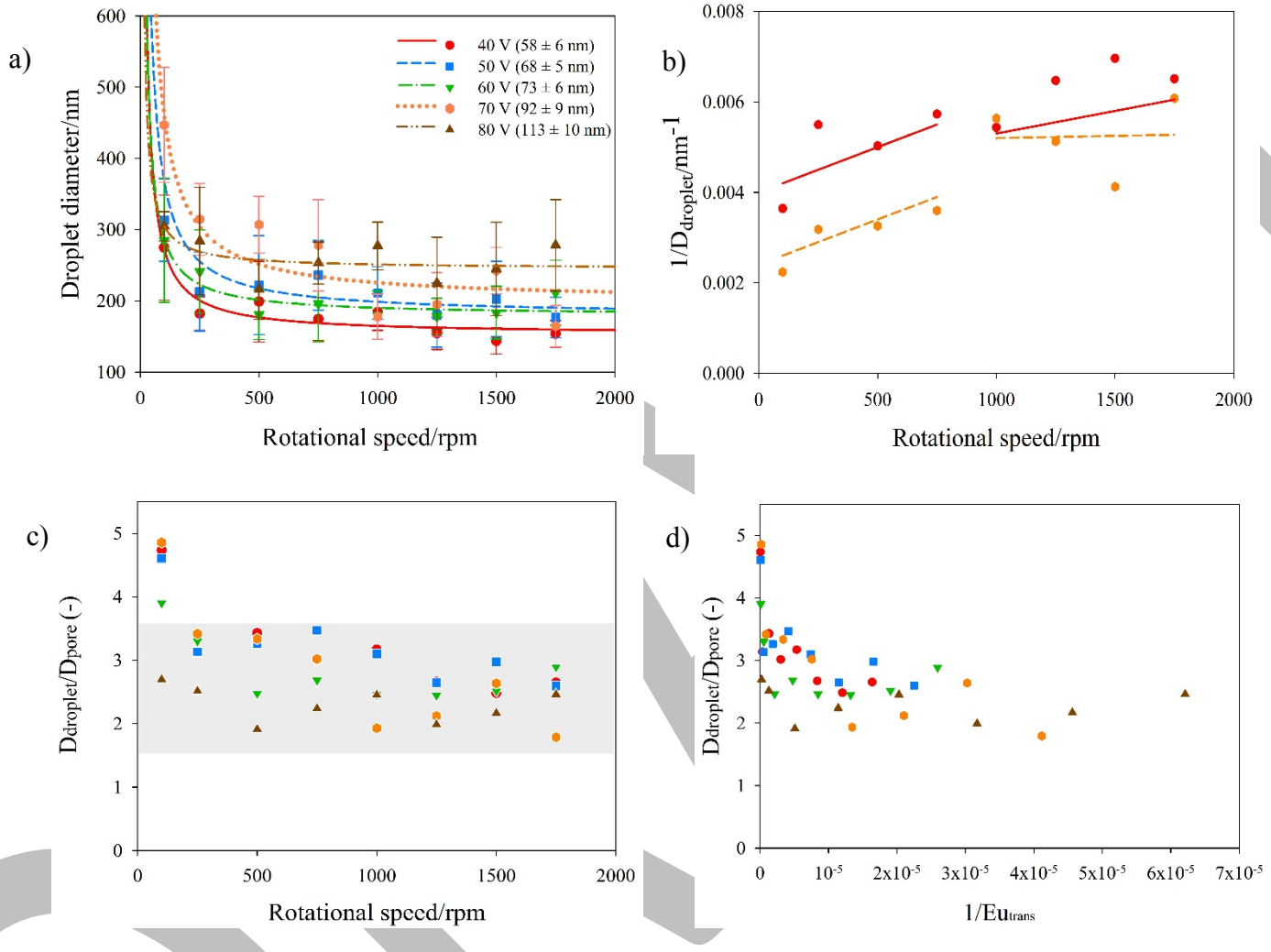

Figure 6. a) Droplet diameter of NEs against the rotational speed, for membranes with different pore sizes with R^2 value of 0.86, 0.69, 0.84, 0.81, 0.38 for a 40, 50, 60, 70 and 80 V membrane, respectively, using an inverse first order fit; b) inverse of the droplet diameter against rotational speed for 40 and 70 V membranes; c) ratio ofdroplet diameter to pore diameter against rotational speed; and d) ratio of droplet diameter to pore diameter against inverse of the Euler number.

3.2.5 Stability of emulsions

The stability of the NEs was evaluated by analysing a sample by DLS at 20 ˚C the same day that it was produced and after twelve days stored at 8 ˚C. The average droplet diameter was 200 ± 30 nm and 207 ± 50 nm in the first and second analysis, respectively. The negligible difference in the droplet size between both analyses suggests that no coalescence occurred during storage.

3.3 Process modelling

Five different models from literature presented in Table 2 were used to estimate the droplet size and compared with experimental values from NEs obtained using a 40 V membrane, using the dimensions described in Figure 1 for the membrane and experimental apparatus.

To estimate the droplet diameter, the shear stress was calculated as described in the introduction section (Eq. 9 and 10). Figure 7 shows the shear stress profile along the membrane radius for different rotational speeds. For each rotational speed, the highest point in the curve represents the critical radius (r_c). The estimated droplet diameter values for each model was calculated using the shear stress value at the critical radius because that will give the lowest droplet diameter that the model can predict. Figure 8 shows a comparison among the experimental and the estimated droplet diameters for the five models for a 40 V membrane. The results are tabulated in Table S4 in the supporting information.

Table 2. Models for the estimation of the droplet size in membrane emulsification based on force or torque balances (all terms defined in the nomenclature)

Balance	Model expression	Reference
$F_\gamma = F_D$ (force)	$D_d = \frac{\sqrt{18\tau^2 r_p^2 + 2\sqrt{81\tau^4 r_p^4 + 4\tau^2 r_p^2 \gamma^2}}}{3\tau}$	
$M_{\gamma z} = F_D \left(\frac{D_d}{2}\right) cos\alpha$ (torque)	$D_d = \frac{12^{1/3}\left[r_p^2\tau^2\left(\gamma + \sqrt{\gamma^2 - 12r_p^2\tau^2}\right)\right]^{1/3}}{3\tau} + \frac{12^{2/3} r_p^2 \tau}{3\left[r_p^2\tau^2\left(\gamma + \sqrt{\gamma^2 - 12r_p^2\tau^2}\right)\right]^{1/3}}$	22
$F_\gamma = F_D$ (force)	$D_d = \sqrt{\frac{2r_p\gamma}{6k_x\tau}}$	19
$F_{st} = F_D$	$\frac{D_d}{D_p} = \left(\frac{2\gamma}{3k_x D_p \tau}\right)^{1/3}$	34
$(F_D + F_B)h = F_\gamma r_p$ (torque)	$\left[6k_x\pi\tau h^2 + \frac{4}{3}\pi r^3(\rho_c - \rho_d)g\right]h = 2\pi\gamma r_p^2$ $\frac{4}{3}\pi r^3 = \frac{\pi}{6}h\left(3r_p^2 + h^2\right)$	20

The first and second model are a force and a torque balance, respectively.[22] For both models, the buoyancy and the inertial forces have been neglected. The droplet diameters show a decrease in the droplet diameter as the shear stress increases, as in the experiments, but a comparison between the experimental values and the theoretical values from both models at the highest rotational speed (1750 rpm) produces an overestimation of 643 % and 170 % of the droplet diameter for the torque and force balance, respectively.

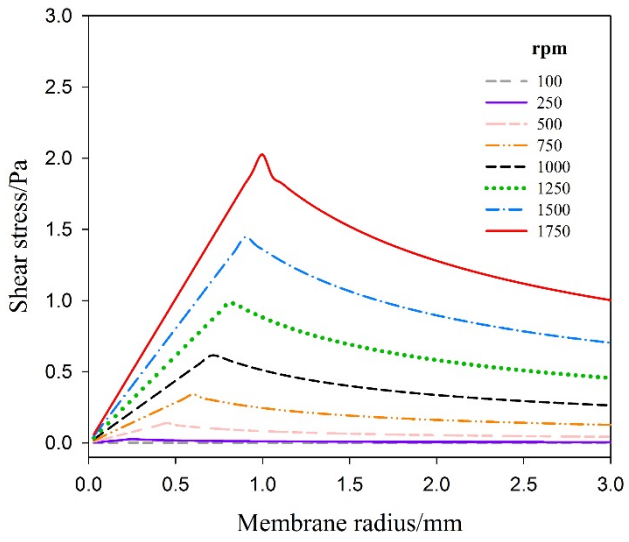

Figure 7. Shear stress profile along the membrane radius at different rotational speeds.

The third model developed by Rayner and Trägårdh [19] as a force balance between interfacial and drag force also leads to an overestimation of the experimental data of 244 % for the highest shear stress. The fourth model proposed by Suárez et al. (2013) estimates the minimum droplet size that could be produced taking into account a force balance between the static pressure force and drag force. The model shows only an overestimation of 155 % at the highest rotational speed.

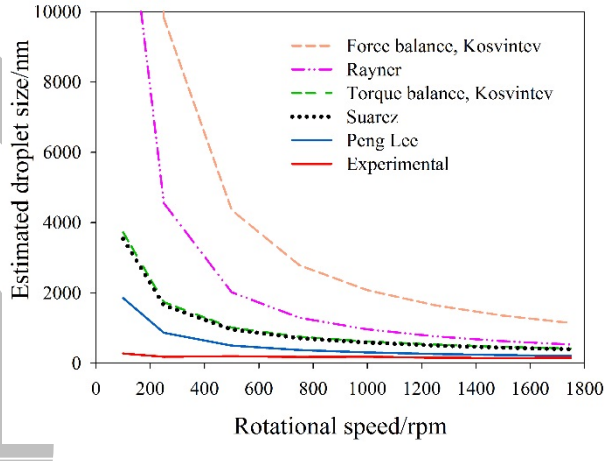

Figure 8. Comparison between droplet size estimations obtained from the four different models and the experimental data for a NEs prepared using a 40 V membrane (58 ± 6 nm).

The similarity observed in Figure 8 between the Suarez model and the torque balance[22] for all the rotational speeds is due to the similar magnitude between the static pressure force and interfacial tension force (See supporting information, Figure S2). All of these models have been developed for emulsions and membrane pore sizes in the micrometer range, giving good results for these larger droplets. On the other hand the fifth model was developed by the authors,[20] for crossflow ME with membrane pores in the nanometer range and is a two equation system where drag, buoyancy and interfacial tension force are considered. This model results in a much smaller overestimation of 34 % at the highest shear rate, providing a better, while not yet ideal, fit with the experimental data.

For the four applied models, the predicted values tend to converge at higher rotational speeds, while larger discrepancies with the experimental values were observed at low rotational speeds. This difference can be attributed to the fact that, at low rotational speed, below 200 rpm, the magnitude of the buoyancy force becomes significant.[18] In addition, the magnitude of the drag force is relatively low and the ratio between these two forces will be smaller. In fact, at the lowest rotational speed, the drag force is just two orders of magnitude higher to the buoyancy force, while at the highest rotational speed the ratio increases to about five orders of magnitude. Furthermore, results in this work here show that at low rotational speeds surfactants play a major role, a factor that is not directly accounted for in any of the models present in the literature. Figure S2 shows the magnitude of each force for both rotational speeds.

4. Conclusions

In the present work, the formation of nanoemulsions by membrane emulsification in a stirred-cell setup using bespoke AAMs is reported for the first time. The AAMs were synthesized under specific experimental conditions to obtain different pore sizes and subsequently tested for different process and surfactant parameters for NE production.

The NE results demonstrated that the addition of a lipophilic and a hydrophilic surfactant in the dispersed and the continuous phase, respectively, was beneficial, especially when the membrane has a small interpore distance. A rapid decrease of the interfacial tension caused by the presence of the surfactant in the dispersed phase led to a reduction of droplet formation time, and monodispersed droplets with smaller droplet size distributions were obtained. When surfactants were added in both phases, the effect of the molecular weight of the surfactant in the continuous phase was significant only at low rotational speeds due to a low mass transfer of the surfactant in the continuous phase to the oil/water interface when the droplet was growing. In ME, a critical aspect is a fast provision of surfactant during the droplet growth step and this was achieved by the incorporation of surfactant in the dispersed phase (due to a small diffusion distance from the bulk of the dispersed phase to the oil/water interphase). Therefore, the effect of the molecular weight of the surfactant in the continuous phase becomes minimal.

The shear stress exhibited a negative correlation with the droplet size and droplet size distribution. The results demonstrated that the smaller the pore size the lower shear stress needed to achieve droplet detachment. As expected, the droplet size was proportional to the pore size, with values of the ratio (D_d/D_p) ranging from 1.8 to 3.5. These low proportionality values are due to the narrow pore size distribution that characterize AAMs, compared to other membranes.

Five droplet size estimation models for ME were compared to experimental data. The five models led to an overestimation of the droplet size, especially at low rotational speeds. A model produced by the authors, which, unlike the others, considers the effects of buoyancy and inertia, produced a better estimation across the entire range of rotational speeds, showing that these forces cannot be ignored at the nanoscale.

Supporting information is available free of charge on the ACS Publication website.

Synthesis conditions for the production of AAMs (Table S1), properties of the synthesized AAMs (Table S2), droplet size of NEs obtained using a 40 V membrane under different surfactant conditions (Table S3), droplet diameter of NEs obtained at for a 60 V membrane under different surfactant conditions (Figure S1), comparison of the experimental NEs obtained with current droplet diameter estimation models (Table S4), magnitude of the different forces acting over a droplet in a stirred-cell setup for ME (Figure S2).

Author information

Corresponding author

*E-mail: dmattia@bath.ac.uk

Notes

The authors declare no competing financial interest.

Acknowledgments

Authors express their gratitude to the Mexican National Council for Science and Technology (CONACYT) for the doctoral scholarship granted to Maria Medina-Llamas.

Abbreviations

AAMs	Anodic alumina membranes
DW	Deionized water
HLB	Hydrophilic-Lipophilic Balance
ME	Membrane emulsification
NEs	Nanoemulsions
SFO	Sunflower oil

Nomenclature

b	blade height (m)
D	impeller diameter (m)
D_s	surfactant diffusion coefficient ($m^2\ s^{-1}$)
D_d	droplet diameter (m)
D_p	pore diameter (m)
D_{dA}	droplet diameter after coalescence (m)
D_{dB}	droplet diameter before coalescence (m)
Eu_{trans}	Euler number (-)
F_B	buoyancy force (N)
F_D	drag force (N)
$F\gamma$	interfacial tension force (N)
F_{st}	Static pressure force (N)
g	gravitational constant (9.81 m s^{-2})
h	droplet height (m)

k	Boltzmann constant (1.380×10^{-23} J K^{-1})
k_s	surfactant mass transfer coefficient (m s^{-1})
k_x	wall correction factor (-)
$M_{\gamma z}$	momentum of the interfacial tension force at pore edge (N s)
M_w	molecular weight of the surfactant (g mol^{-1})
n_b	number of blades (-)
ΔP	transmembrane pressure (Pa)
r_c	critical radius (m)
r_d	droplet radius (m)
r_p	membrane pore radius (m)
Re	Reynolds number (-)
t	droplet formation time (s)
T	temperature of the continuous phase (K)
T_D	tank diameter (m)
v_d	velocity of the dispersed phase within a single pore (m s^{-1})
Greek symbols	
α	angle from the edge pore
γ	interfacial tension (mN m^{-1})
δ	boundary layer thickness (m)
μ	viscosity of the continuous phase (Pa·s)
ρ_c	density of the continuous phase (kg m^{-3})

ρ_d	density of the dispersed phase (kg m^{-3})
τ	shear stress (Pa)
ω	angular speed of the impeller (rad s^{-1})

References

(1) Lovelyn, C.; Attama, A. A., Current state of nanoemulsions in drug delivery. *J Biomater Nanobiotechnol* **2011,** 2, (05), 626.

(2) Wang, L.; Li, X.; Zhang, G.; Dong, J.; Eastoe, J., Oil-in-water nanoemulsions for pesticide formulations. *J. Colloid Interface Sci.* **2007,** 314, (1), 230-235.

(3) Morelli, S.; Holdich, R. G.; Dragosavac, M. M., Chitosan and Poly (Vinyl Alcohol) microparticles produced by membrane emulsification for encapsulation and pH controlled release. *Chem. Eng. J.* **2016,** 288, 451-460.

(4) Pathak, M., Numerical simulation of membrane emulsification: Effect of flow properties in the transition from dripping to jetting. *J. Membr. Sci.* **2011,** 382, (1), 166-176.

(5) Koroleva, M. Y.; Yurtov, E. V., Nanoemulsions: the properties, methods of preparation and promising applications. *Russ. Chem. Rev.* **2012,** 81, (1), 21-43.

(6) McClements, D. J., Edible nanoemulsions: fabrication, properties, and functional performance. *Soft Matter* **2011,** 7, (6), 2297-2316.

(7) Forgiarini, A.; Esquena, J.; González, C.; Solans, C., Formation and stability of nano-emulsions in mixed nonionic surfactant systems. In *Trends in Colloid and Interface Science XV*, Koutsoukos, P., Ed. Springer Berlin Heidelberg: 2001; Vol. 118, pp 184-189.

(8) Piacentini, E.; Figoli, A.; Giorno, L.; Drioli, E., 4.03 - Membrane Emulsification. In *Comprehensive Membrane Science and Engineering*, Elsevier: Oxford, 2010; pp 47-78.

(9) Schubert, H.; Engel, R., Product and Formulation Engineering of Emulsions. *Chem. Eng. Res. Des.* **2004,** 82, (9), 1137-1143.

(10) Charcosset, C.; Limayem, I.; Fessi, H., The membrane emulsification process—a review. *Journal of Chemical Technology & Biotechnology* **2004,** 79, (3), 209-218.

(11) Oh, D. H.; Balakrishnan, P.; Oh, Y.-K.; Kim, D.-D.; Yong, C. S.; Choi, H.-G., Effect of process parameters on nanoemulsion droplet size and distribution in SPG membrane emulsification. *Int. J. Pharm.* **2011,** 404, (1), 191-197.

(12) Gong, J.; Butler, W. H.; Zangari, G., Tailoring morphology in free-standing anodic aluminium oxide: Control of barrier layer opening down to the sub-10 nm diameter. *Nanoscale* **2010,** 2, (5), 778-785.

(13) Masuda, H.; Fukuda, K., Ordered metal nanohole arrays made by a two-step replication of honeycomb structures of anodic alumina. *Science* **1995,** 268, (5216), 1466-1468.

(14) Lee, K. P.; Leese, H.; Mattia, D., Water flow enhancement in hydrophilic nanochannels. *Nanoscale* **2012,** 4, (8), 2621-2627.

(15) Alkire, R. C.; Gogotsi, Y.; Simon, P.; Eftekhari, A., *Nanostructured materials in electrochemistry*. John Wiley & Sons: 2008.

(16) Leese, H.; Bhurtun, V.; Lee, K. P.; Mattia, D., Wetting behaviour of hydrophilic and hydrophobic nanostructured porous anodic alumina. *Colloids Surf. Physicochem. Eng. Aspects* **2013,** 420, 53-58.

(17) Yanagishita, T.; Kawamoto, M.; Nishio, K.; Masuda, H., Preparation of Monodisperse Hydrogel Particles by Membrane Emulsification Using Highly Ordered Anodic Porous Alumina. *Chem. Lett.* **2013,** 42, (11), 1349-1351.

(18) Peng, S. J.; Williams, R. A., Controlled Production of Emulsions Using a Crossflow Membrane: Part I: Droplet Formation from a Single Pore. *Chem. Eng. Res. Des.* **1998,** 76, (8), 894-901.

(19) Rayner, M.; Trägårdh, G., Membrane emulsification modelling: how can we get from characterisation to design? *Desalination* **2002,** 145, (1–3), 165-172.

(20) Lee, K. P.; Mattia, D., Manufacturing of Nanoemulsions Using Nanoporous Anodized Alumina Membranes: Experimental Investigation and Process Modeling. *Ind. Eng. Chem. Res.* **2013,** 52, (42), 14866-14874.

(21) Vladisavljević, G. T.; Schubert, H., Preparation of emulsions with a narrow particle size distribution using microporous α-alumina membranes. *J. Dispersion Sci. Technol.* **2003,** 24, (6), 811-819.

(22) Kosvintsev, S. R.; Gasparini, G.; Holdich, R. G.; Cumming, I. W.; Stillwell, M. T., Liquid-liquid membrane dispersion in a stirred cell with and without controlled shear. *Ind. Eng. Chem. Res.* **2005,** 44, (24), 9323-9330.

(23) Nagata, S., *Mixing: principles and applications*. Halsted Press: 1975.

(24) Koutsou, C. P.; Karabelas, A. J., Shear stresses and mass transfer at the base of a stirred filtration cell and corresponding conditions in narrow channels with spacers. *J. Membr. Sci.* **2012,** 399, 60-72.

(25) Goddeeris, C.; Cuppo, F.; Reynaers, H.; Bouwman, W.; Van den Mooter, G., Light scattering measurements on microemulsions: estimation of droplet sizes. *Int. J. Pharm.* **2006,** 312, (1), 187-195.

(26) Kaszuba, M.; McKnight, D.; Connah, M. T.; McNeil-Watson, F. K.; Nobbmann, U., Measuring sub nanometre sizes using dynamic light scattering. *Journal of Nanoparticle Research* **2008,** 10, (5), 823-829.

(27) Lee, W.; Ji, R.; Gösele, U.; Nielsch, K., Fast fabrication of long-range ordered porous alumina membranes by hard anodization. *Nature materials* **2006,** 5, (9), 741-747.

(28) Jessensky, O.; Müller, F.; Gösele, U., Self-organized formation of hexagonal pore arrays in anodic alumina. *Appl. Phys. Lett.* **1998,** 72, (10), 1173-1175.

(29) O'sullivan, J.; Wood, G., The morphology and mechanism of formation of porous anodic films on aluminium. *P. Roy. Soc Lond. A.* **1970,** 317, (1531), 511-543.

(30) Peng Lee, K.; Mattia, D., Monolithic nanoporous alumina membranes for ultrafiltration applications: Characterization, selectivity–permeability analysis and fouling studies. *J. Membr. Sci.* **2013,** 435, 52-61.

(31) Wagdare, N. A.; Marcelis, A. T. M.; Ho, O. B.; Boom, R. M.; van Rijn, C. J. M., High throughput vegetable oil-in-water emulsification with a high porosity micro-engineered membrane. *J. Membr. Sci.* **2010,** 347, (1-2), 1-7.

(32) Rayner, M.; Trägårdh, G.; Trägårdh, C., The impact of mass transfer and interfacial expansion rate on droplet size in membrane emulsification processes. *Colloids Surf. Physicochem. Eng. Aspects* **2005,** 266, (1), 1-17.

(33) Schröder, V.; Schubert, H., Production of emulsions using microporous, ceramic membranes. *Colloids Surf. Physicochem. Eng. Aspects* **1999,** 152, (1), 103-109.

(34) Suárez, M. A.; Gutiérrez, G.; Coca, J.; Pazos, C., Stirred tank membrane emulsification using flat metallic membranes: a dimensional analysis. *Chem. Eng. Process. Process Intensif.* **2013,** 69, 31-43.

(35) Suárez, M. A.; Gutiérrez, G.; Matos, M.; Coca, J.; Pazos, C., Emulsification using tubular metallic membranes. *Chem. Eng. Process. Process Intensif.* **2014,** 81, 24-34.

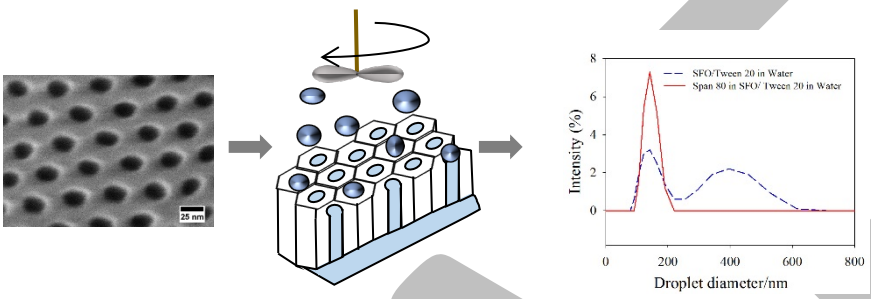
25 nm
SFO/Tween 20 in Water
Span 80 in SFO/ Tween 20 in Water
Intensity (%)
Droplet diameter/nm
0
2
4
6
8
0
200
400
600
800